Validation of geometry modelling approaches for offshore gas dispersion simulations

I. Ahmed[a,b,*], T. Bengherbia[a], R. Zhvansky[a], G. Ferrara[a], J. X. Wen[b], N. G. Stocks[b]

[a] *DNV GL, London, UK*
[b] *Warwick FIRE, School of Engineering, University of Warwick, Coventry, UK*

Abstract

Computational Fluid Dynamics (CFD) codes are widely used for gas dispersion studies on offshore installations. The majority of these codes use single-block Cartesian grids with the porosity/distributed-resistance (PDR) approach to model small geometric details. Computational cost of this approach is low since small-scale obstacles are not resolved on the computational mesh. However, there are some uncertainties regarding this approach, especially in terms of grid dependency and turbulence generated from complex objects. An alternative approach, which can be implemented in general-purpose CFD codes, is to use body-fitted grids for medium to large-scale objects whilst combining multiple small-scale obstacles in close proximity and using porous media models to represent blockage effects. This approach is validated in this study, by comparing numerical predictions with large-scale gas dispersion experiments carried out in DNV GLs Spadeadam test site. Gas concentrations and gas cloud volumes obtained from simulations are compared with measurements. These simulations are performed using the commercially available ANSYS CFX, which is a general-purpose CFD code. For comparison, further simulations are performed using CFX where small-scale objects are explicitly resolved. The aim of this work is to evaluate the accuracy and efficiency of these different geometry modelling approaches.

Keywords: gas dispersion, geometry modelling, computational fluid dynamics

*Corresponding author. E-mail address: irufan.ahmed@ricardo.com (I. Ahmed)

1. Introduction

Hazardous materials being released into the atmosphere is one of the main causes of accidents in oil and gas installations. The accidental release and subsequent dispersion of flammable gases could cause fires and explosions. Therefore, consequence analysis of gas dispersions is crucial when optimizing the location of gas detectors and to determine the risk of fire and explosion.

A number of modelling techniques are used for consequence analysis of accidental gas releases. These include empirical, phenomenological and Computational Fluid Dynamics models. Both empirical and phenomenological models can provide an estimate quickly and are widely used in the oil and gas industry. However, these models have a limited range of validity since they cannot capture the effects of obstacles and complex terrains.

In contrast, CFD models solve the equations of fluid mechanics in three-dimensions, thus, enabling the accurate representation of complex geometries that are often found in oil and gas production facilities. This makes CFD the preferred method to study gas dispersion, especially for offshore oil and gas installations.

However, the use of CFD is not without its own challenges. One of the major drawbacks of CFD is the time taken to generate the computational mesh required for the simulation. The computational and mesh size and, hence, the cost of such simulations will become prohibitively expensive if one were to resolve all geometrical obstacles (pipes, instrumentation, equipment etc.).

Most CFD codes used in the industry (for example FLACS, KFX and EXSIM) employ the porosity distributed resistance (PDR) approach [1], which treats objects smaller than the computational grid (sub-grid objects) as porous medium. The main advantage of the PDR approach is the reduction computational mesh size, which in turn reduces the cost of simulations. However, there are some uncertainties regarding this approach, especially in terms of grid independence and turbulence generated by the sub-grid objects.

An alternative approach for gas dispersion simulations, which can be implemented in a general purpose CFD tool, is to body-fit the grid around large objects whilst combining multiple small-scale obstacles in close proximity and using porous media models to represent blockage effects. A number of such studies can be found in the literature, for example, Gilham et al. [2] carried out a ventilation study of a gas turbine compartment using the commercial CFD package STAR-CD, where small-scale objects were treated as porous

media.

Fothergill et al. [3] estimated the drag on the flow through the porous region used to represent small-scale geometries. This estimate was made by calculating the drag due to each object and obtaining a sum of the overall resistance. This method was implemented in another commercial CFD package called CFX. They compared their results with EXSIM CFD code that uses PDR method and showed that the turbulent kinetic energy and turbulent eddy dissipation predicted by CFX was much lower than EXSIM. The porous model they used simply reduced the volume of free flow and provided extra resistance, but did not generate turbulence. They proposed the inclusion of additional source terms in the turbulence kinetic energy and dissipation equations to account for turbulence generation by the obstacles.

Savvides et al. [4] used FLUENT CFD code to simulate large-scale dispersion of fuel in an offshore module, where small-scale objects were treated as porous media, with the coefficients based on BP data. They showed that this approach can predict gas dispersion with good accuracy. Ivings et al. [5] simulated an under-expanded jet impinging on an array of pipes. In the porous approach, momentum sink terms were included in the fluid flow equations to account for the effect of pipes. They also included turbulence source terms based on the explosion model by Hjertager et al. [6]. Their simulations showed that resolving the objects on the grid did not offer any significant advantages over the porosity based approach.

The main aim of this work is to carry out a validation study of the porosity approach by comparing with large-scale dispersion experiments carried out at DNV GLs Spadeadam test site. In addition comparison is also made with simulations where the small-scale objects are full resolved. The commercial, general purpose CFD package, ANSYS CFX version 15.0 is used for the simulations carried out in this work.

2. Experimental test cases

The experimental test cases chosen for this validation exercise were carried out at DNV GLs Spadeadam test site as part of the Phase 3B project [7]. In these experiments, high pressure natural gas was released inside a test rig until steady-state flow rates were achieved. This rig measured 28 m long, 12 m wide and 8 m high and represented a full-scale offshore module. The structure contained a mezzanine deck at mid-height, with open bar grating.

Gas concentration was monitored at 50 locations inside the test rig using oxygen sensors. The gas concentrations reported by the experiments were when steady-state conditions have been reached. Meteorological conditions such as the ambient wind speed (horizontal component) and direction were measured using an ultrasonic anemometer, mounted at 20 m above ground.

Twenty-three gas dispersion experiments were carried out using two confinement configurations. In this work, only one confinement configuration is considered, in which one side of the module is open and the remaining 3 sides and roof of the module is closed. Two leak scenarios are considered, which are given in Table 1.

Table 1: Two test cases simulated in this work; includes leak properties and atmospheric conditions during the test.

Test case	Leak	Leak	Leak	Orifice	Wind	Wind
case	Location (x, y, z)	direction	rate (kg/s)	diameter (mm)	speed (m/s)	direction (°)
16	5.5,6,1.7	+X	2.6	32.5	0.9	3.66
17	5.5,6,1.7	+X	6.9	32.5	4.2	6.97

The leak location, direction, orifice diameter are identical; the only difference being the leak rate. The wind speed and wind directions are averaged quantities measured during the experiments. Fig. 1 shows the CAD model of the experimental rig with the location of the leaks marked (the two leaks used in this study are pointing along positive x-direction).

3. Numerical setup

3.1. Governing equations

CFD involves the solution of highly non-linear, coupled partial differential equations. These are the equations of mass conservation, Navier-Stokes (momentum conservation) and energy equations. In addition, in dispersion problems one needs to solve additional transport equations for the gas.

Even with the current computational power it is computationally prohibitive to solve these equations directly for most industrial flows; one has to resort to some form of averaging. In this work, the Reynolds-averaged form of the governing equations is used, since it is computationally less expensive and can yield good agreement for time-averaged quantities.

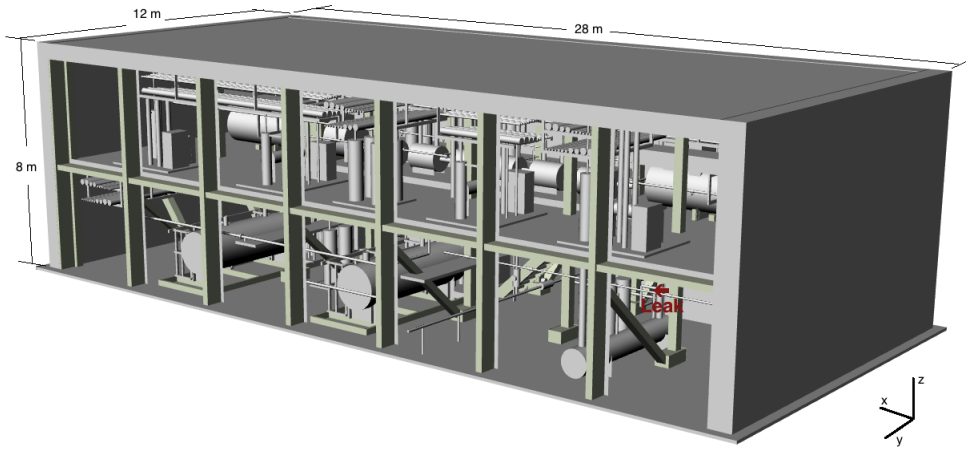

Fig. 1: Experimental rig with dimensions. Location of the leaks are also highlighted in red.

3.2. Turbulence model

Reynolds-averaging the governing equations lead to the famous turbulence closure problem, which requires models to close the equations. A number of turbulence models have been developed over the years, the standard k-ϵ model being the most popular for gas dispersion studies. It is well known that the standard k-ϵ model yields poor results for separated flows, impingement and flows with extra strains [8].

One improvement to the standard k-ϵ model is the Renormalization Group (RNG) k-ϵ model, which is better suited for separated flows and flows around bluff bodies [8]. Therefore, the RNG k-ϵ model is used in this work along with scalable wall functions to model the boundary layer near the walls and the terrain. Note that the default turbulence parameters used in ANSYS CFX v15.0 [9] are used in this work without any modification.

3.3. Geometry and mesh generation

Two geometrical representations of the offshore module with different levels of detail are considered in this work. In the first representation, all small-scale objects are resolved using the computational mesh. This geometry will be referred to as the *resolved* geometry in the rest of the paper. In the second representation, areas with large amount of small-scale objects (for

example piping) are combined to form a porous region. This geometry will be referred to as the *porous* geometry. The cut-off criteria are: any pipe with diameter smaller than 15.24 cm and boxes with cross-sectional area smaller than 232 cm^2 are treated as small-scale objects.

ANSYS ICEM CFD is used to generate the computational meshes for these two geometries. Unstructured tetrahedral mesh generation is used since it is relatively quick to generate a mesh, even for complex geometries. Grid independence studies were performed initially for both geometries to ensure that the results are independent of the grid used. Figures 2(a) and 2(b) respectively show the surface mesh generated for the geometry where all the small-scale objects are resolved and geometry where these small-scale objects are represented using porous regions. Since the leak sizes are different between tests 16 and 17 the meshes generated for these two cases are different as well. The meshes shown in Figure 2 are for test 16. In order to accurately resolve the boundary layers, prism layers are added adjacent to the terrain.

CFX is node based solver, therefore, the number of nodes is the relevant parameter to determine the mesh size. Table 2 shows the mesh sizes for both geometrical representations in each of the two tests. This table shows that the resolved mesh is generally three times larger than the mesh with porous regions.

Table 2: Number of nodes used for the resolved mesh with porous regions.

Test case case	No. of nodes in resolved mesh (in millions)	No. of nodes porous mesh (in millions)
16	3.8	1.1
17	4.5	1.6

3.4. Porosity generation

In the second geometrical representation used in this work, small-scale geometrical objects inside the module (pipework and small structures) are grouped together and the effect of these objects on the fluid flow is determined using a porosity approach. This approach is implemented in this work by including additional source terms in the momentum and turbulence equations. Note that turbulence source terms were ignored in previous studies of Ivings et al. [5] , Fothergill et al. [3] and Gilham et al. [2], whereas these terms are included in this study.

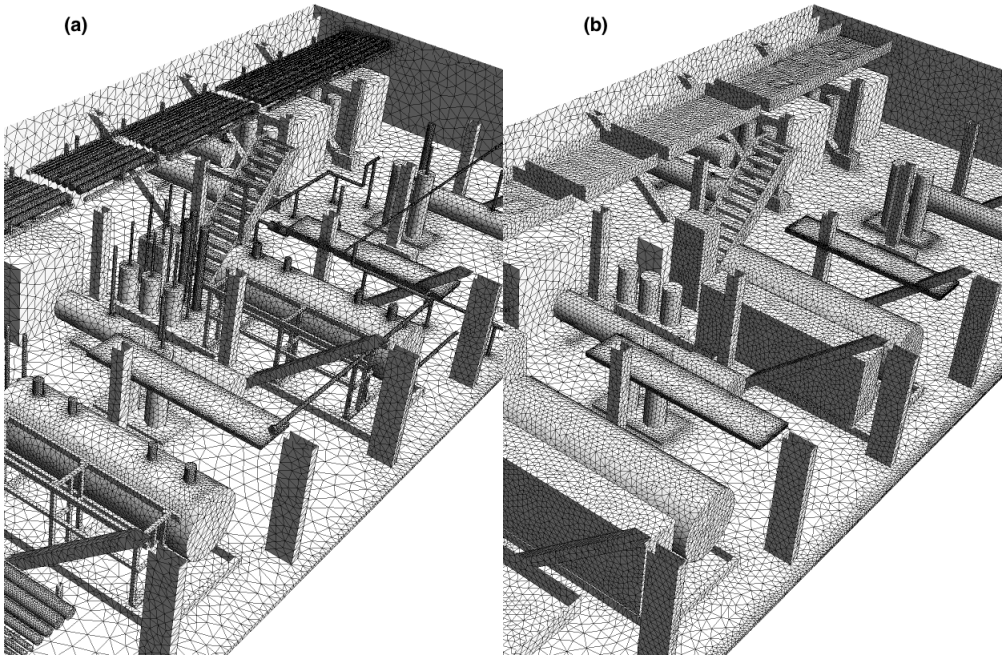

Fig. 2: Surface mesh used for (a) geometry with resolved small-scale objects and (b) mesh with small-scale objects represented using porous regions. Mesh for test case 16 is shown in this figure.

For high Reynolds number turbulent flows one could write the momentum source term as [10]

$$S_i = \frac{1}{2} C_2 \rho |u_i| u_i, \tag{1}$$

where C_2 is the inertial pressure loss coefficient and u_i is the superficial velocity solved using CFD. Similarly, the source terms for turbulence kinetic energy, k, and turbulence dissipation rate, ϵ, are given respectively as

$$S_k = \frac{1}{2} C_2 C_k \rho |u_i|^3, \tag{2}$$

$$S_k = \rho \frac{C_{mu}^{3/4} k^{3/2} - \epsilon}{L}, \tag{3}$$

where L is the turbulence length scale associated with the porous region and in this work it is taken as 10% of the obstacle length in a given coordinate direction, C_k is a turbulence constant and is generally assumed to be independent of the obstacle type [10]. One method of obtaining C_2 is to use the Ergun equation [11], which gives the pressure drop across a packed bed. Using this method C_2 can be given by

$$C_2 = \frac{3.5(1 - p_\epsilon)}{d_p p_\epsilon^3}, \tag{4}$$

where p_ϵ is the porosity and d_p is the particle diameter. Porosity was calculated by determining the volumed blocked by small piping structures in the volume of interest. The directional arrangement of the pipes and small structures means that one cannot assume isotropy for the source terms; instead, different source terms were obtained for the three coordinate directions.

3.5. Initial and boundary conditions

For atmospheric flows, velocity and turbulence profiles need to be defined at the inlet boundaries. The velocity profile by Richards and Hoxey [12] is used in this work, which is given by

$$U(z) = \frac{u_*}{\kappa} \ln \left(\frac{z + z_0}{z_0} \right) \tag{5}$$

where $\kappa = 0.41$ is the von Karman constant, z_0 is the surface roughness, $U(z)$ is the velocity at height z above the ground. The friction velocity is calculated from a reference velocity, U_{ref}, and height, z_{ref}, using

$$k = \frac{u_*^2}{\sqrt{C_\mu}} \tag{6}$$

$$\epsilon = \frac{u_*^3}{\kappa(z + z_0)} \tag{7}$$

3.6. Leak source

Underexpanded jets are created due to high pressure gas releases, i.e. the ratio of exit pressure to the ambient pressure is usually greater than 2 [13]. This creates a series of expansion and compression waves that culminates in a normal shock, which could create repeated patterns depending on the pressure ratio [13].

The gas expansion to atmospheric pressure takes place within a short distance, usually within 10-20 diameters [13]. It is usually unnecessary and prohibitive in terms of computational time to model such level of detail in a gas dispersion study. Often one could use an equivalent source method downstream of the actual leak, where the flow velocity has returned to subsonic levels. Ivings et al. [5] analyzed a number of approaches to represent the leak source. Their results showed that using the pseudo-source approach of Ewan and Moodie [13] gave good agreement with an empirical jet model. In this approach, the pseudo-source is assumed to be sonic, with the mass flow rate and temperature assumed to be the same as the vessel exit conditions but with a larger diameter.

In this work, a resolved subsonic approach is used to obtain the equivalent source, where the jet velocity has decreased to around 200 m/s and the gas concentration has reduced to around 50% due to air entrainment. This equivalent source conditions were determined using DNV GLs PHAST software, which calculates gas dispersion following a discharge from a vessel. It includes air entrainment and gives the centroid velocity, temperature, gas concentration, effective leak diameter downstream of the leak. These values obtained using PHAST for the two leak scenarios considered in this work are shown in 3. The equivalent leak source is located downstream of the actual leak, has a subsonic velocity and the leak diameter is significantly larger than the actual leak. These values are used to create the leak source in CFX, where at least 28 cell faces are used to resolve the leak.

Table 3: Two test cases simulated in this work; includes leak properties and atmospheric conditions during the test.

Test case	Equivalent Leak location (x, y, z)	Centreline concentration (%)	Vapour temperature (K)	Effective diameter (mm)	Centroid velocity (m/s)
16	6.2,6,1.7	49	207	340	186.01
17	6.7,6,1.7	50	188	500	190.28

4. Results and discussion

4.1. Effect of geometry representation

As expected simulations using the geometry with porous regions gives savings in computational time when compared with resolved geometry. For example, for test 16, a steady-state solution was obtained for the resolved geometry using 8 processors in 630 minutes, whereas for the geometry with porous regions a steady-state solution was obtained in 220 minutes. These time savings can be significant when a large number of dispersion simulations are carried. However, it is important to verify whether the results obtained using these two geometry representations are similar.

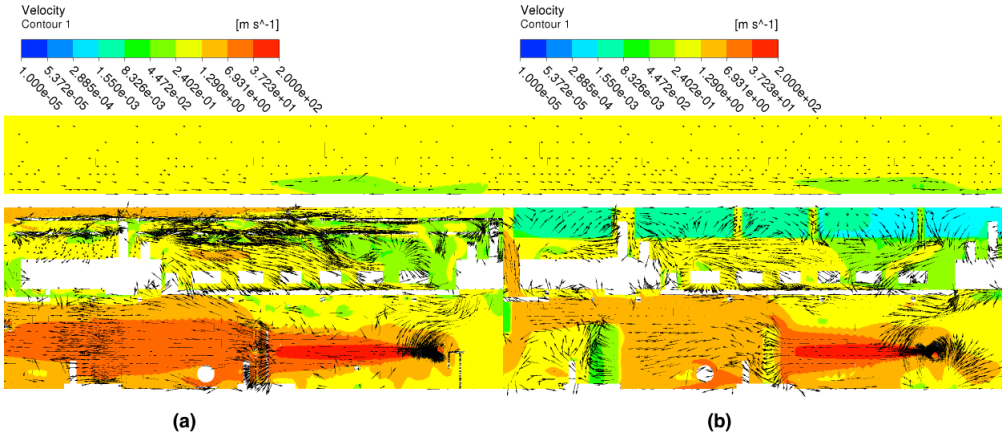

Fig. 3: Contour plots of velocity magnitude: (a) mesh with resolved small-scale objects and (b) mesh with small-scale objects represented using porous regions.

Figure 3(a) and 3(b) show the velocity contours for resolved geometry and geometry with porosity approach for test case 16. Velocity vectors are also

shown on this figure to indicate the flow pattern. These figures show that large-scale flow features are similar for the two geometries. However, one can see differences in the porous regions in terms of both the flow pattern and the velocity magnitude. In the resolved geometry, the flow is predominantly uniform in the region with small-scale piping, whereas when porous regions are used there is some flow re-circulation within the porous regions and the flow velocity is low in these porous regions. In addition, in the resolved geometry a small structure is present roughly 3 meters downstream of the leak. In the porous geometry this structure is represented using a porous box. Figure 3(b) shows that this porous box slows down the flow significantly.

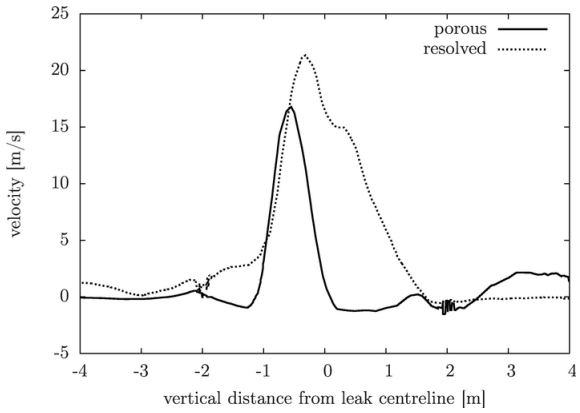

Fig. 4: Vertical velocity profiles downstream of the leak for the two geometry representations.

Fig. 4 shows the velocity profiles along the vertical axis, 9 m downstream of the leak. This figure further shows that the velocity values are higher for the resolved geometry, indicating that there is a momentum loss in the porous domain due to the presence of a porous box.

Figure 5(a) and 5(b) respectively show iso-surfaces of natural gas mass fraction for geometry with all small-scale objects resolved and geometry with porosity regions for test case 16. The iso-surfaces are for natural gas mass fraction of 0.043. These figures show that, for this value of natural gas mass fraction, the clouds inside the module have the same general shape, indicating that the porosity approach is able to predict large-scale flow behavior.

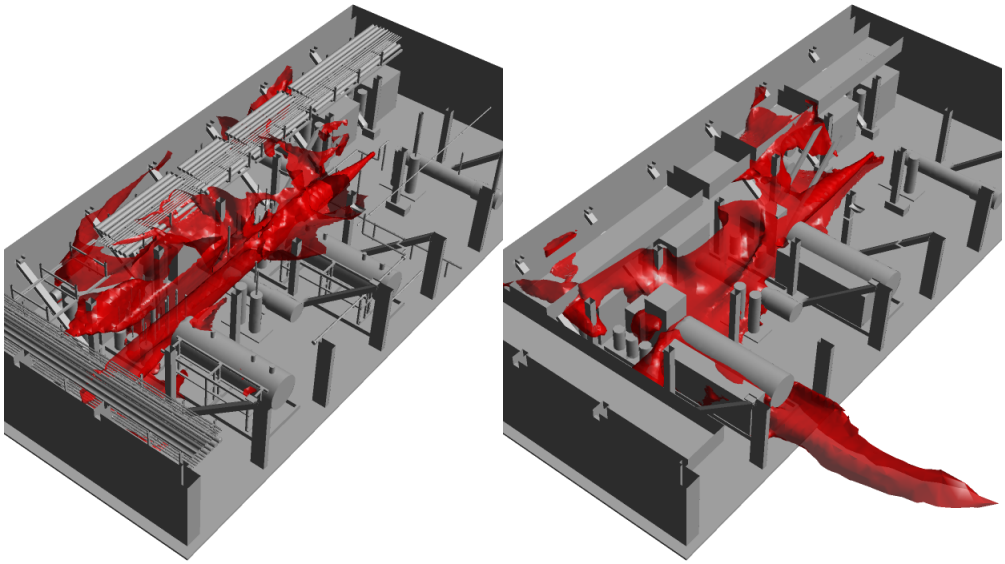

Fig. 5: Iso-surface of natural gas mass fractions of 0.043: (a) mesh with resolved small-scale objects and (b) mesh with small-scale objects represented using porous regions.

4.2. Comparison with experimental data

Figure 6(a) and Figure 6(b) respectively show comparison of natural gas concentrations for the experiments, resolved geometry and geometry with porous regions for the two test cases. Following the observation made my Hansen et al. [14] the gas sensors 46-50, which are moved around inside the module for each test case and located inside the jet plume cannot be trusted and is therefore not used in the post-processing. It can be seen that the numerical results predict the same general trend as the measurements, except for sensor 5, which is just downstream of the actual leak.

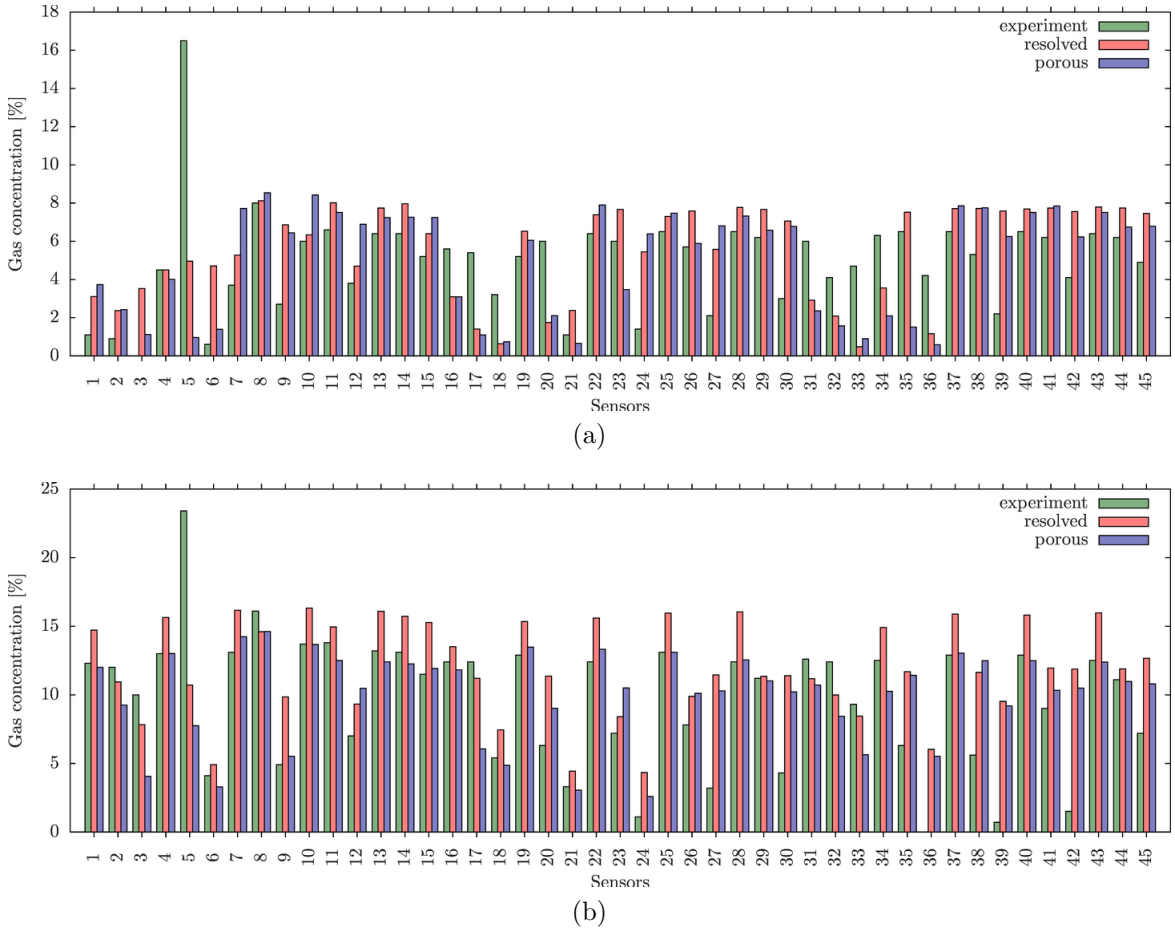

Fig. 6: Comparison of gas concentrations obtained numerically using resolved and porous geometries against measured data. Results are shown for (a) test 16 and (b) test 17.

The results from these simulations show that for majority of the sensor for both test 16 and 17, the differences in concentrations between resolved and porous methods is below 50%. The percentage differences are only large for sensors that recorded a low value. However, there were significant differences between both numerical results and the measured data.

A popular statistical method to compare gas dispersion simulations is to determine the geometric mean and variance for the results, which is shown in Figure 7. A geometric mean and variance of 1 indicates perfect agreement. According to this figure there are significant differences between the measurements and numerical results.

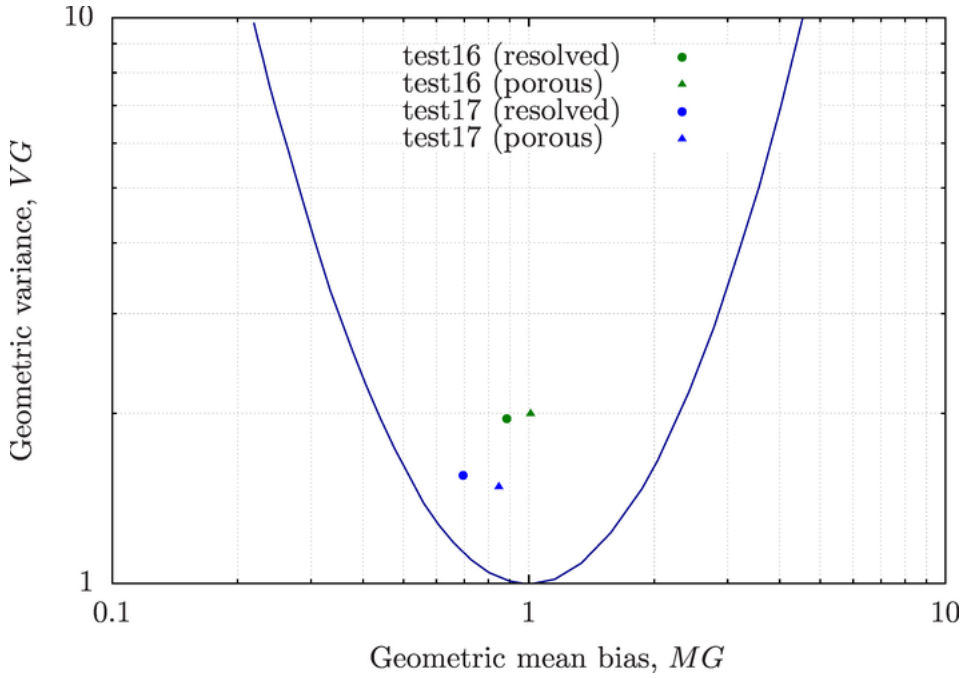

Fig. 7: Geometric mean and variance showing the performance of the 4 simulations with experimental measurements.

Simulating open-air experimental conditions is notoriously difficult due to the changes in the weather conditions. This is likely to be a main cause for the differences observed between measurements and numerical results. For example, in the 4 minutes during which measurements were made for test 16, the wind speed varied between 0.3 m/s to 4.4 m/s and the wind direction

varied between 110° to 210°. Therefore, the assumption of steady-state wind boundary conditions used in this numerical work is questionable and one may have to include transient boundary conditions to accurately predict the wind profile. In addition, the wind speed was only measured at 20 m above ground, and there are no available data for heights below this. Therefore, the wind profile used in the numerical simulations may be significantly different from experiments.

5. Conclusions

Representing small-scale obstacles using the porosity method gives significant savings in computational time, both in terms of mesh generation and flow simulation. The porosity method is able to predict large scale flow features obtained using the resolved geometry and the difference in natural gas concentrations obtained from the majority of monitor points for these two geometries are below 50%.

Therefore, the porosity-based geometry used in this work gives acceptable results when compared with the fully resolved geometry. However, the porosity approach needs to be refined further, which will be the focus of a future study.

The large differences between numerical and experimental results could also be due to the assumption of steady-state wind conditions. Unfortunately in experiments such as the ones considered in this work, the wind direction and speed changes considerably. Ideally, one needs to run a transient simulation with transient boundary conditions to account for this.

Acknowledgements

The authors would like to thank Innovate UK and DNV GL for their financial support in carrying out this research.

References

[1] S. V. Patankar, D. B. Spalding, A calculation procedure for the transient and steady-state behavior of shell-and-tube heat exchangers, McGraw-Hill New York, 1974.

[2] S. Gilham, I. R. Cowan, E. S. Kaufman, Proc. IMechE 213 (1999) 475–489.

[3] C. E. Fothergill, S. Chynoweth, P. Roberts, A. Packwood, J. Loss Prevent. Proc. 16 (2003) 341–347.

[4] C. Savvides, V. Tam, D. Kinnear, in: Major hazards offshore, p. 07489.

[5] M. J. Ivings, M. Azhar, C. Carey, C. J. Lea, S. Ledin, Y. Sinai, C. Skinner, P. Stephenson, Outstanding safety questions concerning the use of gas turbines for power generation–Final report on the CFD modelling programme of work, Health and Safety Laboratory, 2003. Report CM/03/08.

[6] B. H. Hjertager, T. Solberg, K. O. Nymoen, J. Loss Prevent. Proc. 5 (1992) 165–174.

[7] D. M. Johnson, R. P. Cleaver, Gas explosions in offshore modules following realistic releases (Phase 3B)–Final summary report, Advantica Technology, 2001.

[8] C. D. Argyropoulos, N. C. Markatos, Appl. Math. Model. 39 (2015) 693–732.

[9] ANSYS, ANSYS CFX-Solver Theory Guide, ANSYS, Inc., 2013.

[10] N. R. Popat, C. A. Catlin, B. J. Arntzen, R. P. Lindstedt, B. H. Hjertager, T. Solberg, O. Saeter, A. C. Van den Berg, J. Hazard. Mater. 45 (1996) 1–25.

[11] R. B. Bird, W. E. Stewart, E. N. Lightfoot, Transport Phenomena, Wiley, New York, second edition, 2002.

[12] P. J. Richards, R. P. Hoxey, J. Wind Eng. Ind. Aerodyn. 46 (1993) 145–153.

[13] B. C. R. Ewan, K. Moodie, Combust. Science Technol. 45 (1986) 275–288.

[14] O. R. Hansen, S. Bergonnier, J. Renoult, K. van Wingerden, Phase 3B - Lessons learnt from CFD (FLACS-99r2 simulations), GexCon, 2001.